PHYSICAL REVIEW C **89**, 015803 (2014)

Underground study of the $^{17}O(p,\gamma)^{18}F$ reaction relevant for explosive hydrogen burning

A. Di Leva,[1,2,*] D. A. Scott,[3] A. Caciolli,[4,5] A. Formicola,[6,†] F. Strieder,[7] M. Aliotta,[3] M. Anders,[8] D. Bemmerer,[8] C. Broggini,[4] P. Corvisiero,[9,10] Z. Elekes,[8] Zs. Fülöp,[11] G. Gervino,[12] A. Guglielmetti,[13,14] C. Gustavino,[15] Gy. Gyürky,[11] G. Imbriani,[1,2] J. José,[16] M. Junker,[6] M. Laubenstein,[6] R. Menegazzo,[4] E. Napolitani,[17] P. Prati,[9,10] V. Rigato,[5] V. Roca,[1,2] E. Somorjai,[11] C. Salvo,[6,10] O. Straniero,[2,18] T. Szücs,[11] F. Terrasi,[2,19] and D. Trezzi[13,14]

(LUNA Collaboration)

[1]*Dipartimento di Fisica, Università di Napoli "Federico II," Napoli, Italy*

[2]*INFN, Sezione di Napoli, Napoli, Italy*

[3]*SUPA, School of Physics and Astronomy, University of Edinburgh, Edinburgh EH9 3JZ, UK*

[4]*INFN, Sezione di Padova, 35131 Padova, Italy*

[5]*INFN, Laboratori Nazionali di Legnaro, Padova, Italy*

[6]*INFN, Laboratori Nazionali del Gran Sasso, Assergi, Italy*

[7]*Institut für Experimentalphysik, Ruhr-Universität Bochum, Bochum, Germany*

[8]*Helmholtz-Zentrum Dresden-Rossendorf, Dresden, Germany*

[9]*Dipartimento di Fisica, Università di Genova, Genova, Italy*

[10]*INFN Sezione di Genova, Genova, Italy*

[11]*MTA Atomki, Debrecen, Hungary*

[12]*Dipartimento di Fisica Sperimentale, Università degli Studi di Torino, and INFN, Sezione di Torino, Torino, Italy*

[13]*Università degli Studi di Milano, Milano, Italy*

[14]*INFN, Sezione di Milano, Milano, Italy*

[15]*INFN, Roma La Sapienza, Italy*

[16]*Departament de Física i Enginyeria Nuclear, EUETIB, Universitat Politécnica de Catalunya, and Institut d'Estudis Espacials de Catalunya, Barcelona, Spain*

[17]*CNR-IMM MATIS at Dipartimento di Fisica e Astronomia, Università di Padova, Padova, Italy*

[18]*Osservatorio Astronomico di Collurania, Teramo, Italy*

[19]*Seconda Università di Napoli, Caserta, Italy*

(Received 2 August 2013; published 21 January 2014)

Background: The $^{17}O(p,\gamma)^{18}F$ reaction affects the production of key isotopes (e.g., ^{18}F and ^{18}O) in the explosive hydrogen burning that powers classical novae. Under these explosive conditions, the reaction rate is dominated by contributions from a narrow resonance at $E_{c.m.} = 183$ keV and by the combined contributions of direct capture and low-energy tails of broad resonances. At present, the astrophysical reaction rate is not well constrained because of the lack of data in the energy region appropriate to classical novae.

Purpose: This study aims at the measurement of the $^{17}O(p,\gamma)^{18}F$ reaction cross section in order to determine its reaction rate in the temperature region appropriate to explosive hydrogen burning in novae.

Method: The $^{17}O(p,\gamma)^{18}F$ reaction cross section was measured using both the prompt detection of the emitted γ rays and an activation technique. Measurements were carried out at the Laboratory for Underground Nuclear Astrophysics (Gran Sasso, Italy) where the strongly reduced cosmic-ray-induced background allows for improved sensitivity compared to previous studies.

Results: The $^{17}O(p,\gamma)^{18}F$ reaction cross section was measured in the range $E_{c.m.} = 160$ to 370 keV. The strength of the $E_{c.m.} = 183$ keV resonance, $\omega\gamma = 1.67 \pm 0.12\,\mu$eV, was determined with unprecedented precision. The total S factor was obtained through a combined fit of prompt γ-ray and activation results. An overall global fit including other existing data sets was also carried out and a recommended astrophysical reaction rate is presented.

Conclusions: The reaction rate uncertainty attained in this work is now below the required precision for nova models. We verified, following a full set of hydrodynamic nova models, that the abundances of oxygen and fluorine isotopes obtained with the present reaction rate are determined with 10% precision and put firmer constraints on observational signatures of novae events.

DOI: 10.1103/PhysRevC.89.015803 PACS number(s): 23.20.Lv, 26.30.−k, 26.20.Cd, 26.50.+x

I. INTRODUCTION

Novae belong to a more general class of astronomical phenomena, which includes type I x-ray binaries and type Ia supernovae. These events are powered by thermonuclear explosions driven by mass transfer episodes in close stellar binary systems. In the case of classical novae, the system consists of a white dwarf (WD) and a low-mass companion, usually a K or M main sequence star. When the secondary fills its Roche lobe, H-rich material is transferred through the inner Lagrangian point of the system. Since this material

*Corresponding author: antonino.dileva@unina.it

†Corresponding author: alba.formicola@lngs.infn.it

carries angular momentum, it does not fall directly on top of the WD, but forms an accretion disk orbiting around the compact star. Ultimately, a fraction of this material spirals in and piles up on top of the star. Since the accretion rate onto the WD is rather low, $\sim 10^{-10}$ to 10^{-9} $M_\odot$/yr, the H-rich material accumulates under mild degenerate conditions, paving the road for a subsequent thermonuclear runaway. This is characterized by a sudden increase of the brightness by $\sim$10 magnitudes in a few days. The typical maximum luminosity is about 10^4–10^5 $L_\odot$. The decline in luminosity, back to the original level, takes several days to a few months. Following the explosion, most of the accreted material is ejected into the interstellar medium; see reviews in Refs. [1–4].

The maximum temperature attained at the bottom of the H-rich envelope during the outburst depends on the mass and initial temperature (or luminosity) of the WD, the composition of its envelope, and the mass accretion rate. For the most common type of WDs harbouring a C-O core, the maximum temperature ranges between 0.1 and 0.2 GK, while temperatures up to 0.4 GK are developed in case of WDs with O-Ne cores [5]. These temperatures are substantially larger than those attained in hydrostatic H burning.

During the thermonuclear runaway that powers the nova phenomenon, the $^{17}O(p,\gamma)^{18}F$ reaction competes with the faster $^{17}O(p,\alpha)^{14}N$. The $^{17}O(p,\gamma)^{18}F$ reaction leads to the production of ^{18}F and of ^{18}O through its subsequent β^+ decay ($t_{1/2} = 109.77$ min [6]) and contributes to the synthesis of ^{19}F and ^{15}N, through the $^{18}O(p,\gamma)^{19}F$ and $^{18}O(p,\alpha)^{15}N$ reactions, respectively [2,5].

The interest in the $^{17}O+p$ reaction for novae is threefold. First, classical novae are major sources of the galactic ^{13}C, ^{15}N, and ^{17}O [4,5,7,8]. Second, they are well-known galactic dust factories [9]. Indeed, a number of presolar C-rich (i.e., SiC and graphite) grains, presumably condensed in the ejecta from novae, have already been identified in the Murchison and Acfer meteorites [10,11]. Nevertheless, in the ejecta frequently the abundance of O is larger than C, and therefore nova signatures are expected to be identified in some O-rich grains. Third, although no γ rays from classical novae have yet been detected through satellite observations [12], it has been predicted that novae should exhibit prominent emission at 511 keV from β^+ annihilation of ^{18}F. All these aspects require an accurate determination of both $^{17}O(p,\gamma)^{18}F$ and $^{17}O(p,\alpha)^{14}N$ reaction rates with a high degree of accuracy in the temperature range $T = 0.1$–0.4 GK.

In the past decade the $^{17}O(p,\gamma)^{18}F$ cross section, at astrophysical relevant energies, was investigated by several groups. The level scheme of ^{18}F is quite complex, as shown in Fig. 1. The energy region relevant for novae nucleosynthesis is dominated by a narrow resonance located at $E_{c.m.} = 183$ keV and by the direct capture (DC) component. The two broad resonances at $E_{c.m.} = 557$ and 677 keV have to be considered as well, because their low-energy tails contribute appreciably to the cross section. For simplicity, both contributions from the DC and the broad resonances' tails are referred to as the nonresonant contributions hereafter.

The pioneering work of Rolfs [13] investigated the low-energy range by detecting the prompt γ rays and resulted in a constant DC component of $S_{DC} = 9$ keV barn at energies

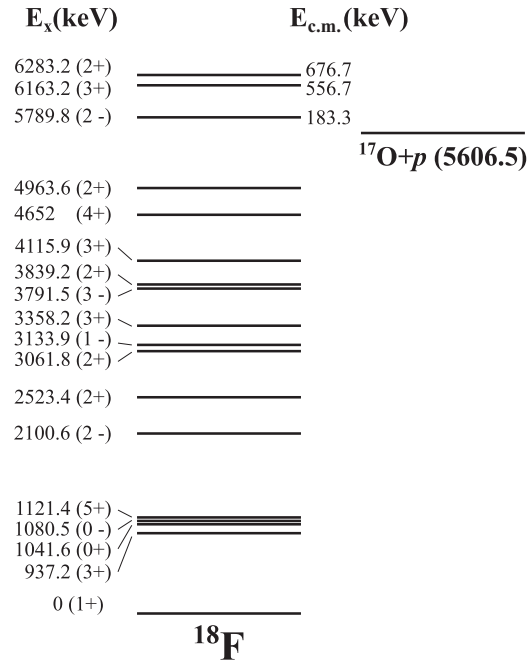

FIG. 1. ^{18}F level scheme; only levels relevant for this work are shown.

relevant for novae.[1] However, Rolfs's lowest energy points display a very different energy dependence compared to subsequent studies, so Fox *et al.* [15] questioned whether those data points were dominated by the DC process or rather affected by the presence of the two broad resonance tails.

Fox *et al.* [15,16] observed for the first time the resonance at $E_{c.m.} = 183$ keV and using the measured spectroscopic factors of 21 bound states derived an S_{DC} about a factor of 2.5 lower than reported in Ref. [13]. The 183-keV resonance strength and the S_{DC} were also determined by Chafa *et al.* [17] counting the ^{18}F decays. The results of these measurements, Refs. [16] and [17], are in significant disagreement, with a difference of about a factor of 2. In 2010, Newton *et al.* [18] performed a measurement covering the energy range $E_{c.m.} = 257$–470 keV. The S_{DC} determination was in good agreement (within 20%) with the estimate of Fox [16].

Recently two other works have been published: a measurement of the total cross section performed through the direct detection, in coincidence with γ rays, of the ^{18}F recoils using the DRAGON recoil separator at TRIUMF [19], and a measurement of the differential cross section at the Nuclear Science Laboratory of the University of Notre Dame [20]. The measurement of Ref. [19] spanned an energy range similar to that in Ref. [18]. The S factor was found to be higher than in Ref. [16]. The discrepancy could arise from

[1]The astrophysical S factor, for a reaction between two nuclei with nuclear charges Z_1 and Z_2 having reduced mass μ, is defined by the equation [14]:

$$\sigma(E) = \frac{1}{E}\exp(-2\pi\eta)S(E),$$

where $\eta = \frac{Z_1 Z_2 e^2}{\hbar}\left(\frac{\mu}{2E}\right)^{\frac{1}{2}}$ is the Sommerfeld parameter.

unobserved transitions in Ref. [16] and/or an inappropriate subtraction of the DC in either Ref. [16] or Ref. [17]. Kontos *et al.* [20] addressed their work to constrain the high-energy resonances and the DC contribution. The authors performed measurements of the differential cross section of individual primary transitions in the energy range $E_{c.m.} = 345$–1700 keV at several angles. Additionally the resonance strengths of the two broad resonances at $E_{c.m.} = 557$ and 677 keV as well as of other narrow resonances were determined. The S factor energy dependence of Ref. [20] agrees with the low-energy data of Ref. [18].

The purpose of the present work is to solve the existing discrepancies in the $^{17}O(p,\gamma)^{18}F$ S-factor determination using two complementary measurement techniques. We reported on the results of the experimental determination of the resonant and nonresonant contribution to the total cross section in Ref. [21]. Here, together with the details of the measurements, we also present the results of additional measurements that give the cross section below the $E_{c.m.} = 183$ keV resonance, Sec. II, and of the analysis, Secs. III and IV. The determinations of the reaction rate and the related uncertainty at the astrophysical relevant energies are discussed in Sec. V. The evaluation of its impact on the novae nucleosynthesis is presented in Sec. VI.

II. EXPERIMENTAL TECHNIQUES

The unique low background environment of the underground Gran Sasso National Laboratory (LNGS) allowed the high-accuracy measurement of the $^{17}O(p,\gamma)^{18}F$ reaction cross section. The measurements were performed using two independent approaches: the prompt γ-ray detection and the off-line counting of ^{18}F decays from irradiated targets (hereafter, activation method).

The experiment was performed at the underground LUNA 400-kV accelerator [22] in the energy interval $E_{c.m.} =$ 160–370 keV. A proton beam with a typical intensity of 200 μA was delivered on solid targets. The beam passed through a copper pipe extending to within 2 mm from the target (see Fig. 2). The pipe was cooled to liquid nitrogen temperature and served as a cold trap to prevent carbon buildup. A negative voltage of 300 V was applied to the cold trap to suppress secondary electrons. The isolated target holder served as a Faraday cup for beam integration with a precision of about 3%.

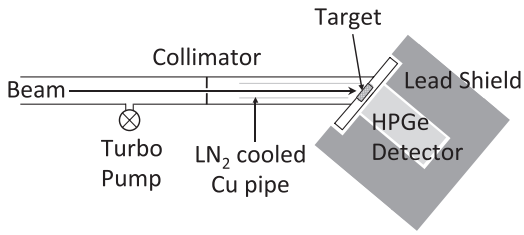

FIG. 2. Sketch of the experimental setup used for the prompt γ-ray detection, consisting of a HPGe detector placed in close geometry to the target, tilted at an angle of 55° with respect to the beam axis.

For the measurements Ta_2O_5 targets were used. The target parameters (thickness, stoichiometry, isotopic enrichment) and their behavior under intense beam bombardment have a strong influence on the experimental results. The production and characterization of the targets are extensively discussed in Ref. [23]. Briefly, targets of about 27 keV thick at 151-keV proton energy, with typical enrichments of 31% in ^{16}O and 65% in ^{17}O and 4% in ^{18}O, were prepared by anodic oxidation of tantalum backings in isotopically enriched water. The targets were monitored during measurements through nuclear resonant reaction analysis (NRRA) by observing the yield of the $E_p = 151$ keV resonance in $^{18}O(p,\gamma)^{19}F$. Stoichiometric and isotopic stability of the targets under intense proton beam was proved through Rutherford backscattering (RBS) measurements at INFN Laboratori Nazionali di Legnaro and secondary ion mass spectrometry (SIMS) measurements at Dipartimento di Fisica e Astronomia, Università di Padova. The maximum accumulated charge on target was limited to 25 C, corresponding to at most a 20% degradation in target thickness.

A. Prompt γ-ray setup

The deep underground environment of LNGS leads to a reduction of the background events by a factor of 2500, with respect to surface measurements, in the energy region between 3 and 7 MeV [24], where mainly the primaries and the ground-state transitions of the $^{17}O(p,\gamma)^{18}F$ reaction are expected. To improve the signal-to-background ratio in the energy range below 3 MeV the detector was surrounded with a 10-cm-thick lead shielding, obtaining an additional reduction of natural radioactivity background by a factor of 10.

A 115% relative efficiency HPGe detector, placed at an angle of 55° with respect to the beam axis, was used to collect the prompt γ rays. The center of the detector front face was at a distance of 1.5 cm from the center of the target, as schematically shown in Fig. 2.

Thus, target and detector front face were parallel so that angular distribution effects are minimized. The sensitivity of the detector setup to an angular distribution with a $P_2[\cos(\vartheta)]$ term (see, e.g., Fox *et al.* [16]) was tested with a GEANT4 [25] based simulation. For this purpose we used the experimental angular distribution data of Kontos *et al.* [20] for the primary transition to the $E_x = 937$ keV state at $E_{c.m.} \sim 400$ keV. The difference in the detection efficiency with respect to an isotropic angular distribution is well below the present statistical uncertainty.

The γ-ray detection efficiency was determined using standard calibrated ^{137}Cs and ^{60}Co sources and was extended to higher energies measuring the yield of the well-known $^{14}N(p,\gamma)^{15}O$ resonance at $E_{c.m.} = 259$ keV. Due to the close geometry of the detector, corrections for significant true coincidence summing effects have to be applied. For this reason the efficiency measurements were carried out at several detector-to-target distances, i.e., 1.5, 6.5, 16.5, and 21.5 cm, and the data were simultaneously fit following the procedure described in Refs. [26,27]. The summing-in and summing-out corrections to the number of observed counts are calculated

from the formulas

$$N_{\rm gs} = Y\left(b_{\rm gs}\eta_{\rm fe}(E_{\rm gs}) + \sum_i b_i \eta_{\rm fe}\left(E_{i_{\rm sec}}\right)\eta_{\rm fe}\left(E_{i_{\rm pri}}\right)\right), \quad (1)$$

$$N_{i_{\rm pri}} = Y b_i \eta_{\rm fe}\left(E_{i_{\rm pri}}\right)\left[1 - \eta_{\rm tot}\left(E_{i_{\rm sec}}\right)\right],$$

$$N_{i_{\rm sec}} = Y b_i \eta_{\rm fe}\left(E_{i_{\rm sec}}\right)\left[1 - \eta_{\rm tot}\left(E_{i_{\rm pri}}\right)\right], \quad (2)$$

where Y is the total number of reactions and b_i is the ith γ-ray branching ratio. The photopeak and total efficiencies, $\eta_{\rm fe}$ and $\eta_{\rm tot}$ respectively, are defined as in Ref. [26] and include the fitting parameters. The labels gs, pri, and sec refer to ground-state, primary, and secondary transitions, respectively. These equations assume isotropic angular distributions [28] and no angular correlation between the γ rays. Throughout this work secondary branching ratios are taken from Ref. [29].

B. Activation setup

Since ^{18}F β^+ decays to the ground state of ^{18}O it is possible to determine its activity through the detection of the 511-keV γ ray from the positron annihilation. Targets used solely for the activation measurements were irradiated for several hours in order to saturate the ^{18}F activity, using the same experimental setup of the prompt γ-ray measurements. The target profile was measured before and after each irradiation.

The loss of ^{18}F by backscattering, estimated using a GEANT4-based simulation, was found to be well below 1% at all bombarding energies and was thus neglected. Unfortunately, the short half-life of ^{18}F prevents a direct measurement of backscattering losses, but the simulation used had been validated during the ^{3}He$(\alpha,\gamma)^7$Be study [30] through the direct measurement of backscattering losses of the longer-lived ^{7}Be.

The activated targets were transferred to the subterranean low level assay (STELLA), the LNGS low background counting facility [31]. The positron annihilation γ-ray counting was performed with a HPGe detector (p-type coaxial, 85.5% relative efficiency) surrounded by a massive 4π lead/copper shielding [innermost layer of 5 cm of detachable oxygen-free high conductivity (OFHC) copper, on the outside 25 cm of Pb]. The shielding is enclosed in a polymethylacrylate box, continuously flushed with nitrogen in order to prevent any contamination from radon. The detector background at 511 keV is approximately 0.1 counts h^{-1}, negligible compared to the counting rate from the activated targets, ∼25 to 5 counts h^{-1} at the lowest measurement energy. The targets were placed in front of the detector end cap at a distance of 13 mm. A Ta absorber was interposed between target and detector to fully stop the emitted positrons. The absolute efficiency $\eta_{\rm Act}$ of the detector was determined with a calibrated ^{85}Sr source, which emits a single γ ray of 514 keV. This allowed a direct determination of the efficiency at the energy of interest free of coincidence summing effects. The influence of ^{18}F spatial distribution was investigated with the GEANT4-based simulation toolkit MAGE [32]. The code was validated comparing the simulations of a ^{85}Sr and a ^{137}Cs source with measurements, and the agreements were within 2.2% and 1.3%, respectively. The results for the dependence of $\eta_{\rm Act}$ on the spatial distribution (pointlike centered source compared with extended source and dislocation from the center of the Ta target) gave a maximal variation of 4%. These results have been taken into account by summing the uncertainties in the overall efficiency uncertainty.

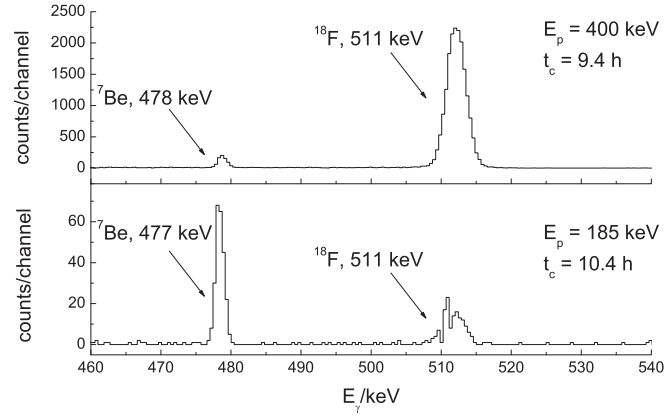

FIG. 3. Activation γ-ray spectra acquired after irradiations at $E_p = 400$ and 185 keV. The 478-keV peak originates from the decay of ^{7}Be produced by the ^{10}B$(p,\alpha)^7$Be reaction on B impurities in the target.

Spectra were recorded every 20 min over a period of several hours in order to follow the decay of ^{18}F. Figure 3 shows the relevant part of two activation γ-ray spectra taken on targets irradiated at the highest and lowest studied energies. In both cases the 511-keV peak is indicated as well as the ^{7}Be decay peak most likely produced by the ^{10}B$(p,\alpha)^7$Be reaction. A half-life analysis confirmed that the observed 511-keV peak belongs to ^{18}F. Typical 511 keV counting rates as a function of time are shown in Fig. 4 along with an exponential fit. After several half-lives the counting rate reached the background level, proving that no longer-lived positron emitters were present. In the case of some higher energy irradiations, a weak, fast decaying component was observed. Most likely this originated from ^{11}C ($t_{1/2} = 20.4$ min) or ^{13}N ($t_{1/2} = 9.96$ min) produced by proton capture reactions on B and C impurities in the target, respectively.

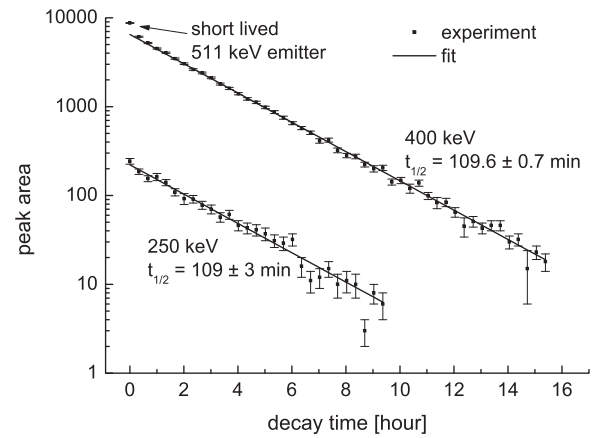

FIG. 4. Typical decay curves of ^{18}F. They refer to the $E_p = 400$ and 250 keV irradiation energies. The fitted half-life is in excellent agreement with the literature value, proving that the 511-keV peak is due exclusively to ^{18}F.

III. EXPERIMENTAL PROCEDURE AND ANALYSIS

A. Off-resonance *S* factor

Measurements were performed in the energy range $E_{\text{c.m.}} =$ 160 to 370 keV.

The off-resonance reaction yield $Y_{\text{off},i}$ for the ith transition, at laboratory proton energy E_0, was derived assuming that the S-factor variation over the target thickness Δ_{lab} is negligible:

$$Y_{\text{off},i} = N_{\text{inc}} b_i \int_{E_0-\Delta_{\text{lab}}}^{E_0} \frac{\sigma(E)}{\varepsilon(E)} dE$$

$$= N_{\text{inc}} b_i S_{\text{exp}}(E_{\text{c.m.}}) \int_{E_0-\Delta_{\text{lab}}}^{E_0} \frac{\exp\left(-2\pi Z_1 Z_2 \sqrt{\frac{m_p}{E}}\right)}{\frac{m_{17_O}}{m_{17_O}+m_p} E\varepsilon(E)} dE,$$

where N_{inc} is the number of incident particles, b_i is the branching ratio for the ith transition, ε is the effective stopping power calculated using SRIM tables [33], and $E_{\text{c.m.}}$ is the energy in the center-of-mass framework corresponding to the effective interaction energy

$$E_{\text{eff}} = \frac{\int_{E_0-\Delta_{\text{lab}}}^{E_0} E\sigma(E) dE}{\int_{E_0-\Delta_{\text{lab}}}^{E_0} \sigma(E) dE}.$$

1. Prompt γ-ray measurements

Measurements of the prompt γ-ray yield were performed at several energies. The yield of the primary transitions was determined following the γ-line shape analysis method presented in Ref. [26]. The summing-out corrections range between 15% and about 30% depending on the complexity of the γ-ray cascade. The analysis of the primary transitions to some states was hampered by natural background. In these cases the corresponding S factor was determined through secondary transitions that are unique for the particular cascade, namely the $E_\gamma = 730$ and 1691 keV lines for the transition from $E_x = 3791$ keV state, the $E_\gamma = 1054$ keV line from the $E_x = 4116$ keV state, and the $E_\gamma = 3531$ keV line from the $E_x = 4652$ keV state. The results agreed within the experimental uncertainties at those energies where both analyses could be performed. A sample γ-ray spectrum for an off-resonance measurement is shown in Fig. 5 (lower panel). S factors are listed in Table I and shown in Fig. 6. At the lowest measurement energy only the strongest primary transition, $R/DC \rightarrow 937$, could be observed. The large energy gap in the experimental data around 330 keV is due to intense beam-induced background produced by a strong resonance in $^{19}F(p,\alpha\gamma)^{16}O$ that prevented a reliable analysis of the spectra. It is worth noting that all quoted S-factor values are based on observed yields and are not estimated from interpolations. The only exception is the transition $R/DC \rightarrow 4652$: at beam energies where the corresponding signal was not observed because of background, its contribution was estimated at the level of 0.1 keV b, in agreement with the analysis of other transitions involving the 4652-keV state.

A total of 16 secondary transitions were analyzed, except for a few cases, due to the sporadic overlapping with beam-induced background. The summing-out correction requires the feeding probabilities to the different levels, which were taken from the primary transition analysis.

The 937 keV $\rightarrow$ 0 transition is the strongest secondary transition, occurring in about 71% of the reactions, after a summing-out correction of about 30%. All transition intensities are listed in Table II. Note that no secondary transitions could be analyzed for the measurement at $E_{\text{c.m.}} =$ 202 keV because of the non-negligible contribution from the $E_{\text{c.m.}} = 183$ keV resonant yield, which could only be

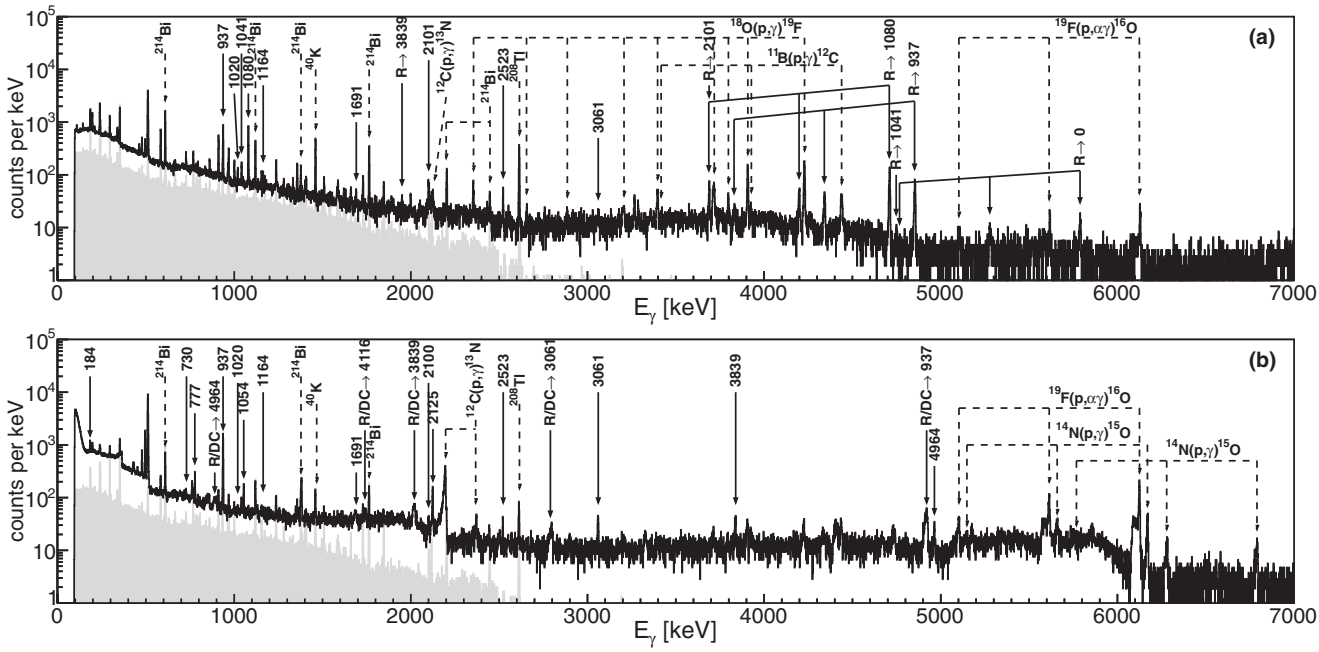

FIG. 5. (a) Sample spectrum of an on-resonance measurement at energy $E_{\text{c.m.}} = 183$ keV. (b) Sample spectrum for an off-resonance measurement at $E_{\text{c.m.}} = 250$ keV. In gray is the time-normalized room background with 10 cm of lead surrounding the detector.

TABLE I. S factors of primary transitions in units of keV barn. The $R/DC \rightarrow 3791,4116$, and 4652 levels are determined from secondary transitions. $R/DC \rightarrow 2100$ and 3133 are not included in S_{Tot}, while for the $R/DC \rightarrow 4652$ a constant value of 0.1(1) keV barn was used where unobservable; see text for details.

$E_{\mathrm{c.m.}}$ (keV)	$R/DC \rightarrow 937$	$R/DC \rightarrow 1120$	$R/DC \rightarrow 2100$	$R/DC \rightarrow 2523$	$R/DC \rightarrow 3061$	$R/DC \rightarrow 3133$
167	2.7(1.0)					
202	2.11(18)	0.25(16)		0.29(10)	0.79(13)	
210	2.1(3)	0.5 (3)		0.29(19)	0.39(16)	
228	2.05(19)	0.35(17)		0.16(8)	0.57(10)	
238	2.00(15)	0.61(14)		0.27(7)	0.68(9)	
250	2.32(11)	0.49(10)	0.08(5)	0.19(5)	0.66(7)	0.06(4)
258	2.33(12)	0.45(11)		0.19(7)	0.66(8)	
274	2.39(11)	0.72(10)		0.09(5)	0.62(5)	
301	3.2(2)	0.6 (2)		0.36(10)	0.73(12)	
359	3.4(3)	0.84(18)	0.07(7)	0.45(9)	0.86(9)	
370	3.6(3)	0.8 (3)		0.51(9)	0.91(9)	0.14(7)

$E_{\mathrm{c.m.}}$ (keV)	$R/DC \rightarrow 3791$	$R/DC \rightarrow 3839$	$R/DC \rightarrow 4116$	$R/DC \rightarrow 4652$	$R/DC \rightarrow 4964$	S_{Tot}[a]
202	0.4(3)	1.26(15)	0.58(15)	0.2(2)	0.53(17)	6.4(6)
210	0.4(4)	1.50(19)	0.48(18)		0.24(7)	6.1(7)
228	0.2(2)	1.37(13)	0.58(11)		0.50(12)	5.9(5)
238	0.4(2)	1.16(11)	0.50(18)	0.1(1)	0.58(10)	6.3(5)
250	0.4(2)	1.10(7)	0.54(6)		0.56(6)	6.4(4)
258	0.5(2)	1.36(10)	0.71(8)		0.53(9)	6.8(4)
274	0.34(10)	1.40(6)	0.53(5)	0.10(4)	0.47(5)	6.7(4)
301	0.33(18)	1.34(11)	0.80(9)	0.19(11)	0.24(9)	7.7(5)
359	0.44(14)	1.9 (3)	0.66(6)		0.51(6)	9.2(5)
370	0.53(14)	1.82(18)	0.67(7)	0.10(7)	0.57(6)	9.5(6)

[a]Target thickness uncertainties included; see Ref. [23] for details.

disentangled for the primary transitions, using the γ-line shape analysis.

The sum of the S factor of the secondary transitions proceeding to the ground state, which is directly comparable with the results of the primary transition analysis, is shown for comparison in Fig. 6. Given the complex ^{18}F decay scheme the fair agreement between primary and secondary transitions is remarkable. A small systematic difference that may be present could arise from the sum of weak, unobserved ground-state transitions of some excited states in ^{18}F.

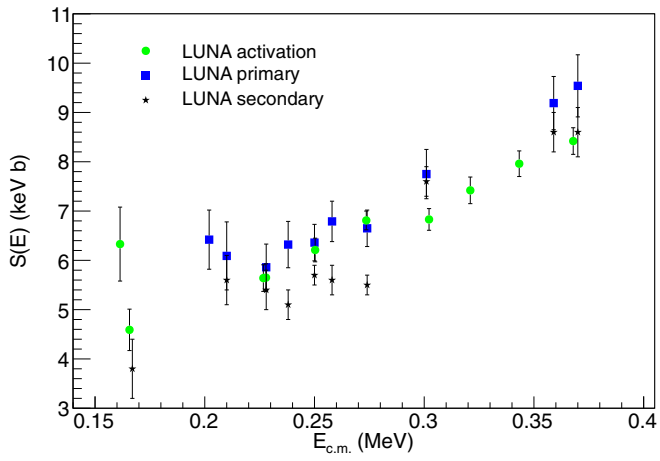

FIG. 6. (Color online) The total S factor of $^{17}\mathrm{O}(p,\gamma)^{18}\mathrm{F}$ reaction as measured in the present work. The filled squares (blue online) are prompt primary γ rays, circles (green online) are activation, and stars are the sum of the secondary transitions to the ground state. The shown uncertainties are of statistical origin only. The differences between the primary and activation data sets are are within their noncommon systematic uncertainties (see text).

2. *Activation measurements*

With the activation method the S factor was determined at 10 energies, and the results are listed in Table III.

The integral of the measured spectrum N_{t_1,t_2} in the time interval (t_1,t_2) is related to the cross section by the equation [34]:

$$N_{t_1,t_2} = \eta_{\mathrm{Act}} \frac{Y_{\mathrm{off}}}{\lambda_{^{18}\mathrm{F}}} (e^{\lambda_{^{18}\mathrm{F}} t_0} - 1)(e^{-\lambda_{^{18}\mathrm{F}} t_1} - e^{-\lambda_{^{18}\mathrm{F}} t_2}),$$

where $\lambda_{^{18}\mathrm{F}}$ is the ^{18}F decay constant and t_0 the irradiation time; $t = 0$ is given by the start of the irradiation.

A ^{13}N contamination, typically 1% of the total rate at the start of a counting period, was taken into account by either including it in the fit or by excluding the first 60 min of counting from the analysis. The results obtained were the same in both cases.

The total S factor reported in Fig. 6 demonstrates the robustness of the experimental approach and the data analysis. The data of all three analyses, primary and secondary prompt γ-ray and activation technique, are in excellent agreement. All three data sets are affected by a series of systematic uncertainties listed in Table V. Some of these uncertainties

TABLE II. S factor for individual secondary transitions in units of keV barn. The numbers in parentheses in the header row indicate the transition energy in keV. S_{Tot} is given by the sum of the transitions proceeding to the ground state, where missing the weighted average of the values at $E_{c.m.} > 220$ keV was assumed.

$E_{c.m.}$ (keV)	937 → 0 (937)	1080 → 0 (1080)	1121 → 937 (184)	2100 → 0 (2100)	2100 → 937 (1164)	2100 → 1080 (1020)	2523 → 0 (2523)	3061 → 0 (3061)	3061 → 937 (2125)
167	2.7(4)						0.4(4)	0.6(6)	2.1(9)
210	4.0(2)	0.10(9)	0.8(3)	0.07(7)	0.3(3)	0.17(17)	0.12(9)	0.33(17)	1.2(2)
228	3.93(14)	0.15(7)	0.8(2)	0.10(6)		0.07(7)	0.23(6)	0.32(14)	1.2(3)
238	3.79(15)	0.06(5)	0.71(17)	0.10(5)	0.14(7)	0.08(6)	0.08(5)	0.22(6)	1.32(15)
250	4.32(7)	0.03(3)	0.94(10)	0.11(3)		0.05(4)	0.15(3)	0.37(5)	1.25(7)
258	4.18(9)	0.12(5)	0.83(13)	0.10(5)	0.26(7)	0.08(6)	0.12(4)	0.39(7)	1.32(7)
274	4.25(8)	0.06(3)	0.87(9)		0.10(5)	0.09(7)	0.12(3)	0.35(4)	1.36(15)
301	5.37(11)	0.11(5)	0.71(15)		0.12(8)	0.18(7)	0.19(5)	0.48(15)	1.66(12)
359	6.49(10)	0.09(4)	0.88(13)	0.13(5)	0.17(10)	0.18(5)	0.24(5)	0.56(14)	
370	6.44(11)	0.11(3)	0.94(13)	0.07(4)	0.17(6)	0.09(5)	0.16(4)	0.57(12)	1.7(2)

$E_{c.m.}$ (keV)	3791 → 2100 (1691)	3791 → 3061 (730)	3839 → 0 (3839)	3839 → 3061 (777)	4116 → 3061 (1054)	4652 → 1121 (3531)	4964 → 0 (4964)	S_{Tot}[a]
167		0.6(6)			1.0(8)			3.8(6)[b]
210			0.7(2)	0.63(19)	0.74(17)			5.6(5)
228	0.09(9)	0.10(10)	0.48(15)	0.80(12)	0.56(10)		0.23(11)	5.4(4)
238		0.19(10)	0.40(11)	0.76(11)	0.50(17)	0.05(5)	0.42(12)	5.1(3)
250			0.34(6)	0.67(6)	0.53(9)			5.7(2)
258	0.37(7)	0.10(8)	0.37(13)	0.49(8)	0.71(8)		0.32(10)	5.6(3)
274	0.19(4)	0.15(6)	0.35(9)	0.73(6)	0.52(5)	0.08(3)	0.29(7)	5.5(2)
301	0.17(8)	0.16(9)	0.51(14)	0.96(9)	0.77(9)	0.16(10)		7.6(3)
359	0.24(7)	0.20(8)	0.49(10)	1.23(8)	0.65(7)		0.61(16)	8.6(4)
370	0.33(7)	0.20(7)	0.78(13)	1.17(8)	0.66(6)	0.08(5)	0.49(14)	8.6(5)

[a]Target thickness uncertainties included; see Ref. [23] for details.
[b]Calculated from 937-keV transition assuming 71% probability.

are common to both approaches while others, e.g., detection efficiencies, have to be treated individually.

B. Resonance strength determination

Using the thick target formalism, a resonance strength can be expressed in terms of the reaction yield as [34]

$$Y_{R,i} = N_{inc}\frac{\lambda^2}{2}\frac{1}{\varepsilon(E_R)}b_{R,i}\omega\gamma \quad , \tag{3}$$

where λ is the de Broglie wavelength at resonance energy E_R, and $b_{R,i}$ is the branching ratio of the ith transition.

TABLE III. Activation method off-resonance S factor.

$E_{c.m.}$ (keV)	S (keV barn)
161	6.3 ± 0.8
166	4.6 ± 0.4
227	5.6 ± 0.3
228	5.7 ± 0.3
250	6.2 ± 0.2
274	6.81 ± 0.19
302	6.8 ± 0.2
321	7.4 ± 0.3
343	8.0 ± 0.3
368	8.4 ± 0.3

1. *Prompt γ-ray results*

The resonance strength and the branching ratios of the 183-keV resonance were determined from measurements with a total charge of 95 C accumulated over several runs of typically 10 C each. The statistics in a single run was insufficient for a reliable estimate of the weak branching ratios.

A sample spectrum on the 183-keV resonance is shown in Fig. 5. In previous studies of the corresponding 2^+ state at 5790 keV, only the two strongest transitions through the ^{18}F states at 937 and 1081 keV could be observed. Thanks to the sensitivity achieved underground, several additional transitions could be observed; see Table IV. For the transition $R \rightarrow 2101$ the peak overlaps with the second escape peak of the stronger transition $R \rightarrow 1080$. The contribution of this latter was estimated, and subsequently subtracted from the $R \rightarrow 2101$ peak, using the relative intensity ratio between full-energy peak and first- and second-escape peaks for a transition of a similar energy.

A number of states populated by the 183-keV resonance are also fed by nonresonant processes. This contribution has to be subtracted from the observed yield. Thus, the nonresonant yield was estimated for each transition by interpolating the off-resonance S factor scaled by the ratio between the experimental resonant peak width and the target thickness.

The counts observed in each transition were corrected for true coincidence summing as discussed in Sec. II A. Since the

TABLE IV. Branching ratios for all observed primary transitions from the $E_{\mathrm{c.m.}} = 183$ keV resonance.

Transition	This work	Literature [35]
$R \rightarrow 0$	2.9 ± 0.4	
$R \rightarrow 937$	24.5 ± 0.8	40 ± 8
$R \rightarrow 1041$	3.4 ± 0.4	
$R \rightarrow 1080$	40.8 ± 0.7	60 ± 8
$R \rightarrow 2101$	11.8 ± 0.8	
$R \rightarrow 2523$	5.5 ± 0.6	
$R \rightarrow 3134$	4.3 ± 0.4	
$R \rightarrow 3358$	2.3 ± 0.3	
$R \rightarrow 3791$	4.5 ± 0.4	

primary transitions' branching ratios required for this calculation are not known a priori, they must be extracted consistently with the summing correction. Therefore, the branchings are free parameters in a global χ^2 fit which takes into account all of the transitions simultaneously. The nominal number of counts N_i^{fit} for a particular primary transition i is calculated directly from Eqs. (1) and (2), where Y is determined by the thick target yield, Eq. (3). A least-squares minimization of all N_i^{fit} values and the corresponding observed counts for each transition results in branching ratios that most accurately reflect the data. The values of the on-resonance branchings $b_{R,i}$ are reported in Table IV.

However, in this procedure a large number of runs obtained from different targets, i.e., with small variations in the isotopic composition and target consumption, were summed. This does not affect the branching ratios, but the resonance strength obtained from the minimisation is not the most accurate but an effective value. Thus, the final resonance strength was calculated from a single run with a fresh target, for which the ^{17}O abundance was determined to be $66.1 \pm 0.5\%$ with SIMS measurements [23]: $\omega\gamma = 1.70 \pm 3\%_{\mathrm{stat}} \pm 7.7\%_{\mathrm{syst}}\ \mu$eV. The systematic uncertainties are summarized in Table V.

TABLE V. Systematic uncertainties (in percentages) for both on-resonance and off-resonance measurements.

Prompt γ	
Photo-peak efficiency	3.5
Relative efficiency (slope)	1.5
Summing	1.5
Activation	
Backscattering	1
Nonresonant subtraction (affects only $\omega\gamma$)	3
^{13}N contaminants	1
η_{Act}	2.5
Common	
Target thickness (affects only off-resonance S factor)	3.8
Charge collection	3
Stopping power	4
Stoichiometry	3
^{17}O abundance	3

2. *Activation results*

The analysis of the decay counting spectra was performed as explained in Sec. III A 2. To determine the resonance strength from the detected ^{18}F decays we used

$$N'_{t_1,t_2} = \eta_{\mathrm{Act}} \frac{Y_{\mathrm{off}} + Y_{\mathrm{R},i}}{\lambda_{^{18}\mathrm{F}}} (e^{\lambda_{^{18}\mathrm{F}} t_0} - 1) \times (e^{-\lambda_{^{18}\mathrm{F}} t_1} - e^{-\lambda_{^{18}\mathrm{F}} t_2}),$$

where Y_{off} is the contribution of the nonresonant yield, where a constant S factor of 5.5 ± 0.5 keV barn was used, as determined by the fit to the off-resonance measurements described in Sec. IV. Several irradiations, for a total of 55 C, were performed at the resonance energy. The weighted average of the results is $\omega\gamma = 1.65 \pm 1.8\%_{\mathrm{stat}} \pm 7.8\%_{\mathrm{syst}}\ \mu$eV. The systematic uncertainties (Table V) are the same as for the off-resonance study except for the target thickness, which in case of a thick target measurement affects only the nonresonant correction of the experimental yield.

The detection efficiency is independent for the two measurement methods, while uncertainties on beam intensity, stopping power, and isotopic abundance are common. Combining the results obtained with the two different techniques, taking into account the common systematic uncertainties, we quote a final resonance strength of

$$\omega\gamma = 1.67 \pm 0.12\ \mu\mathrm{eV}.$$

This result has the highest precision to date and is about 28% higher and 32% lower than the previous values of Ref. [16], $\omega\gamma = 1.2 \pm 0.2\ \mu$eV, and Chafa *et al.* [17], $\omega\gamma = 2.2 \pm 0.4\ \mu$eV, respectively. However, one has to consider that Fox *et al.* observed only two primary transitions, which according to the present work (see Table IV) yield about 65% of the total strength. Correcting their result for the new branching ratio leads to a resonance strength in good agreement with the present work. The strength of Chafa *et al.* is consistent with the present work because of its large uncertainty. We recommend the use of the present work value for the strength of the $E_{\mathrm{c.m.}} = 183$ keV resonance, since the averaging with the result of Chafa would only marginally change the $\omega\gamma$ value and the overall uncertainty would remain unchanged with respect to the present work.

IV. ANALYSIS OF THE NONRESONANT *S* FACTOR

A. The total astrophysical *S* factor

The nonresonant S factor plays a crucial role in the novae temperature range and should be known with high accuracy in the energy region 100–450 keV. The present analysis of the ^{17}O$(p,\gamma)^{18}$F reaction provides a robust global fit for the novae energy region, taking into account all available literature data. The result of this analysis is compared to an analysis of the LUNA data sets only, e.g., the activation and the primary data, as presented in Ref. [21].

The data were analyzed in a common fit procedure with the phenomenological approach already described in Ref. [21] and applied also in Refs. [16,36]. The analysis includes a DC contribution as well as two resonances at

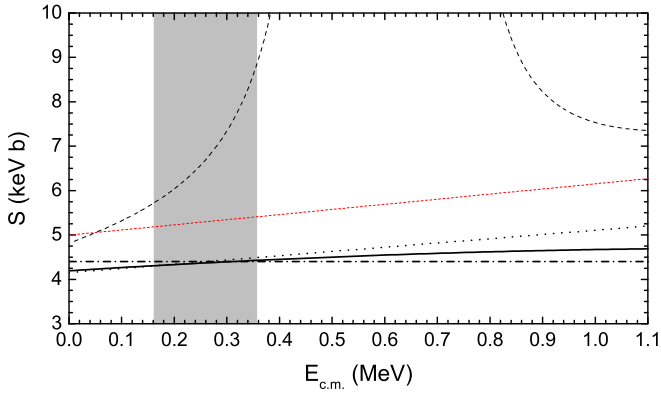

FIG. 7. (Color online) The DC contributions in different analyses. The solid line represents the energy dependence as calculated by Fox *et al.* [16] (here scaled by a factor 1.12; see Table VI). The dotted-dashed line shows a constant DC term as used in Refs. [18] as well as in [21], and the dotted line is the nonresonant energy dependence of Ref. [20] normalized to the other lines in the center of the studied energy range indicated by the shaded area. The thin (red online) dashed line is the original (unscaled) nonresonant contribution of Kontos *et al.* [20]. The latter is the sum of the DC component and a background pole. For comparison the total S factor from the present analysis including the additional contribution from the two broad resonances is plotted (dashed line).

$E_{\mathrm{c.m.}} = 557 (J^\pi = 3^+)$ and 677 keV (2^+). The cross sections of these resonances were calculated in the broad resonance formalism taking into account the energy dependence of the partial widths involved (see, e.g., Ref. [14]). To constrain the broad resonances we used the experimental information from Ref. [20], the γ widths $\Gamma_{\gamma,557} = 0.634 \pm 0.085$ eV and $\Gamma_{\gamma,677} = 1.39 \pm 0.17$ eV, as well as the proton widths $\Gamma_{p,557} = 14.1 \pm 0.3$ keV and $\Gamma_{p,677} = 11.3 \pm 0.2$ keV. Interference effects have been neglected since only minor effects on the cross section are expected where they appear.

In Kontos *et al.* [20] an appropriate fit in the R-matrix formalism required an introduction of a background pole. The background pole usually corrects for unresolved resonance contributions at higher energies but often influences the astrophysical energy region due to its low-energy tail. However, the energy dependence of the background pole tail and the DC contribution at these energies are very weak and cannot be determined from low-energy measurements.

The DC contributions in various analyses are shown in Fig. 7 compared to the total S factor. It is evident that the exact energy dependence is of minor importance in the energy range exploited in this work. For the present analysis we followed the approach of Fox *et al.* [16] and scaled their parametrization of the DC contribution, e.g., a second-order polynomial (see Eq. (15) in Ref. [16]).

In an analysis of different data sets the treatment of systematic errors, i.e., normalization uncertainties such as detection efficiency, stopping power, and proton beam current measurement, becomes very important. The normalization uncertainties determine a correlation between the data sets and may result in a biased estimate if neglected in the fitting procedure. A proper treatment of normalization uncertainties is to fit uncorrelated data obtained by dividing each data set by an independent scaling factor [37,38]. These scaling factors should be fitted simultaneously in a modified least squares fit as discussed in [39] with

$$\chi^2 = \sum_i \left(\sum_j \frac{(f(x_{i,j}) - c_i y_{i,j})^2}{(c_i \sigma_{i,j})^2} + \frac{(c_i - 1)^2}{\sigma_{c_i}^2} \right) + \frac{(\Gamma_{\gamma,557,\mathrm{fit}} - \Gamma_{\gamma,557,\mathrm{lit}})^2}{\sigma_{\Gamma_{\gamma,557}}^2} + \frac{(c_{\mathrm{stop}} - 1)^2}{\sigma_{\mathrm{stop}}^2}, \quad (4)$$

where $y_{i,j}$ represents the jth data point of the ith data set and $\sigma_{i,j}$ is its uncertainty. The parameter c_i represents the scaling factor of the ith data set, with an expectation value equal to 1 and a standard deviation σ_{c_i} equal to the corresponding relative systematic (normalization) uncertainty of the ith data set. Similarly, when different data sets are affected by the same uncertainty, the scaling is factorized into two contributions, i.e., an independent parameter and a second parameter common to both data sets. In the case of the two LUNA data sets, these scaling factors are c_{act}, c_{prim}, and c_{com}, and the corresponding systematic uncertainties are listed in Table V.

Additional fit parameters are the scaling of the DC contribution and the partial γ width of the 557-keV resonance. The former parameter was unconstrained in the fit while the latter was constrained by the literature information from Ref. [20] and treated as the scaling factors in the χ^2 fit [Eq. (4)].[2] The influence of the second broad resonance on the fit quality was extremely small and, thus, $\Gamma_{\gamma,677}$ was fixed to the literature value [20]. The stopping power is a common quantity to most data sets and therefore was also treated independently through the parameter c_{stop}.

In a first step the fit procedure was applied to the LUNA data only. The χ^2 for the best fit is $\chi^2 = 18.4$ for 20 data points and six fit parameters. However, only one of these fit parameters is unconstrained and reduces the number of degree of freedom. The results are summarized in Table VI and the corresponding best fit is shown in Fig. 8. It is worth noting that, with the present approach, the significant correlation between the DC component and the γ width of the 557-keV resonance hampers a precise determination of the true physical resonance width. Therefore, in Table VI only best fit values without uncertainties are reported to allow a reproduction of the calculation.

In a next step the LUNA activation and primary data were fitted together with the data of Newton *et al.* [18] and Hager *et al.* [19]. The low-energy data of Rolfs [13] were

[2]In the present analysis the term *constrained* refers to fit parameters that are allowed to vary from 0 to infinity but are included in the χ^2 expression, i.e., values closer to the literature value or the expectation value, respectively, give smaller contributions to the total modified χ^2.

TABLE VI. Summary of the fit parameters for the two analyses and resulting S-factor values at $E_{\text{c.m.}} = 0$ and 400 keV.

Parameter	Systematic uncertainty[a] (%)	Analysis	
		LUNA only	All data sets
$\Gamma_{\gamma,557}$ (eV)	12.8 (13.4)[b]	0.679	0.588
DC parameter[c]		1.128	1.196
c_{act} (activity data)	2.9	1.013	1.012
c_{prim} (primary data)	4.1	0.962	0.964
c_{com} (LUNA common)	6.4 (7.6)	0.976	0.973
c_{Newton} ([18])	8.1 (9.0)		1.085
c_{Hager} ([19])	9[d]		0.959
c_{stop} (stopping power)	4.0	1.000[e]	1.008
S(0) (keV b)		4.8 ± 0.4	5.0 ± 0.3
S(400) (keV b)		10.4 ± 0.9	10.0 ± 0.8

[a]Value used to constrain the χ^2 fit.
[b]Value in parentheses includes stopping power uncertainty.
[c]Scaling parameter with respect to Eq. (15) in Ref. [16].
[d]Due to the different nature of the experiment an estimate of the common systematic uncertainties is difficult [40], so a similar value as in the other studies was assumed here.
[e]No sensitivity to this parameter (see text for details).

not included in this global analysis since no information on their systematic uncertainty is available. In order to avoid a correlation between the resonance parameters and the low-energy data points of Kontos *et al.* [20], the latter were also excluded from the fit. In any case, due to their large statistical uncertainties, these data would only marginally constrain the fit. The details of Ref. [18] are available from Ref. [41], where the quoted 9% systematic uncertainty for all the data points includes stopping power, detection efficiency, and target thickness. The systematic uncertainty[3] was subtracted quadratically from the uncertainty of the data points quoted in Ref. [18], separating the statistical uncertainties for the fit procedure.

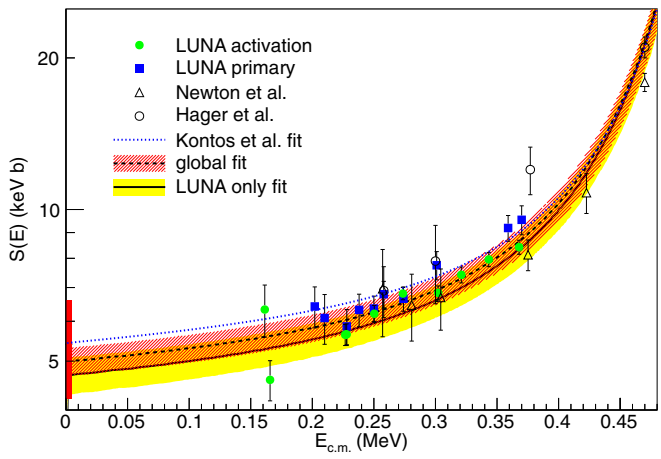

FIG. 8. (Color online) The total S factor of $^{17}\text{O}(p,\gamma)^{18}\text{F}$ at astrophysical energies. The best fit of LUNA only (global) analysis including the 68% confidence limit is shown as solid (dashed) line and shaded (hashed) area, respectively. For comparison the dotted line shows the best fit of the R-matrix analysis of Kontos *et al.* [20] and the red (gray) bar at low energies indicates the total uncertainty of their extrapolation to $S(0)$.

The study of Hager *et al.* [19] was conducted in inverse kinematics and therefore relies on different stopping power values. As a consequence this data set, with an estimated systematic uncertainty of 9%, is completely independent from the other data.

The global fit of these four data sets leads to a best fit with $\chi^2 = 29.1$ for 30 data points and eight fit parameters; again only one parameter effectively reduces the number of degrees of freedom. This global fit (see Table VI and Fig. 8) leads to a lower value for the γ width of the 557-keV resonance, $\Gamma_{\gamma,557} = 0.588$ eV, but still in agreement with the recent result from Ref. [20]. This parameter is mainly constrained by the two data points around $E = 470$ keV which have a comparatively high statistical precision. Note that for both analyses, i.e., the global fit and LUNA only, the stopping power was also coupled to an additional scaling parameter, but since only the data of Hager *et al.* [19] are independent from this parameter, there is basically no sensitivity to a variation of the stopping power and the parameter remained unchanged (see Table VI). However, the stopping power uncertainty correlates the S-factor values to $\Gamma_{\gamma,557}$ and, thus, affects the determination of the total uncertainty.

The uncertainty of the total S factor in the present analysis was obtained from a Monte Carlo procedure: A large number of pseudodata sets were generated from the original data points, i.e., Gaussian distributed with the original value and the quoted uncertainty as mean and standard deviation, respectively. Similarly, a scaling factor was assigned to each data set from the corresponding systematic uncertainty through a Gaussian distribution with mean value equal to unity. Subsequently, a least squares fit was performed on each pseudodata set. The S factor at each energy, obtained in this procedure, is well described by a Gaussian distribution and the uncertainty was determined from a symmetric 68% confidence interval. In this procedure only the treatment of the two broad resonances was slightly modified: The critical parameters, $\Gamma_{\gamma,557}$ and $\Gamma_{\gamma,677}$, were also generated from a Gaussian distribution with a mean as obtained in the present analysis (see Table VI) and the literature uncertainty as standard deviation, e.g., taken from Ref. [20]. The γ-width values obtained in this randomization were kept fixed and were not varied as free parameter in the fit. The resulting uncertainty band for both analysis types, global and LUNA only, are shown in Fig. 8.

In the novae energy range, the difference between the results of the two analyses is rather small and the uncertainty bands are largely overlapping (Fig. 8). The best fit of the LUNA-only analysis results in a larger value for $\Gamma_{\gamma,557}$ than the global

[3]As in the present study we assume a 4% stopping power uncertainty for the data of Ref. [18]. Since this quantity is treated independently, it was subtracted quadratically from the quoted systematic uncertainty, resulting in a value of 8%.

fit. This difference reflects that the γ width of the 557-keV resonance is presently not very well constrained either by the low-energy data or by the independent determination of the resonance strength of Ref. [20]. The evaluation of the covariance matrix of the fit indeed confirms a large correlation between $\Gamma_{\gamma,557}$ and the scaling parameter of the nonresonant contribution. Thus, the resulting S factor depends neither significantly on the precise strengths of the broad resonances at 557 and 677 keV nor on the exact shape and absolute strength of the nonresonant contribution. A determination of these quantities is beyond the scope of the present work and we do not assign an uncertainty to their values. This includes the asymptotic normalization coefficients (ANC), which are usually used to express the DC contribution (e.g., see Ref. [20]). These ANC values cannot be obtained with sufficient precision in the present study. Nevertheless, the total S factor in this energy region is very well constrained by the experimental results of the present experiment.

The observed difference between the present total S factor and the extrapolation of [20] (see Fig. 8) might arise either from the systematic uncertainties of both experiments—note the discrepancy is within the independent systematic uncertainties—or from a different strength and/or energy dependence of the background pole adopted in the analysis of Kontos *et al.* [20]. This small ambiguity cannot be clarified by a common analysis of both experiments.

B. Individual primary transitions

The analysis of the individual primary transitions was performed similarly to the analysis of the total S-factor data. In order to be consistent within the LUNA data sets, the results of the LUNA-only analysis outlined in the previous section were used. In particular, the S-factor values of each primary transition (Table I) were scaled with the corresponding normalization factors, $c_{\rm prim} = 0.962$ and $c_{\rm com} = 0.976$. The total strength of the 677-keV resonance and the branching ratios of both broad resonances were fixed to the values from Kontos *et al.* [20], while for the 557-keV resonance the γ-width value obtained before, $\Gamma_{\gamma,557} = 0.679$ keV, was used.

TABLE VII. The extrapolation to S(0) for the individual primary transitions and a comparison with literature.

Transition	LUNA		Kontos *et al.* [20]	
	S(0) (keV b)	(%)	S(0) (keV b)	(%)
R/DC → 937	1.48 ± 0.08	30.8	1.7 ± 0.3	31.4
R/DC → 1121	0.47 ± 0.05	9.8	0.66 ± 0.13	12.2
R/DC → 1700			0.013 ± 0.002	0.2
R/DC → 2523	0.12 ± 0.03	2.5	0.17 ± 0.03	3.1
R/DC → 3062	0.59 ± 0.03	12.2	0.66 ± 0.10	12.2
R/DC → 3791	0.20 ± 0.05	4.2	0.032 ± 0.005	0.6
R/DC → 3839	0.92 ± 0.04	19.2	0.93 ± 0.14	17.2
R/DC → 4115	0.50 ± 0.03	10.5	0.55 ± 0.08	10.2
R/DC → 4652	0.10 ± 0.03	2.0	0.21 ± 0.03	3.9
R/DC → 4964	0.43 ± 0.03	8.9	0.49 ± 0.07	9.0

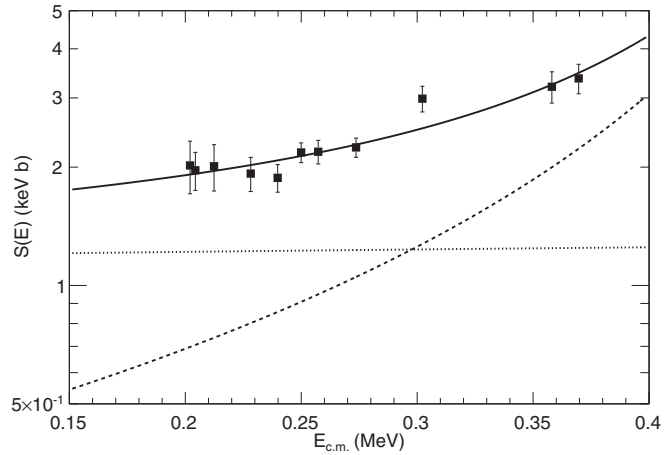

FIG. 9. The astrophysical S factor of the strongest primary transitions R/DC → 937 keV is given in the upper panel, while the other individual primary transitions are shown in the lower panels. The solid lines represent the best fit, while the dotted and dashed lines are the contribution of the DC and the broad resonances, respectively.

The results of the extrapolation to $S(0)$ are shown in Table VII and compared to the analysis of Ref. [20]. The absolute values from the present analysis are lower than the data of Ref. [20] and scale approximately with the difference in the total S factor. In general, the relative contribution of each transition to the total $S(0)$ agree very well with the Kontos *et al.* [20] results. We observed only minor differences for some individual transitions, e.g., for the transition $R/DC \rightarrow 3791$ keV. This particular discrepancy is not surprising since in Kontos *et al.* [20] only

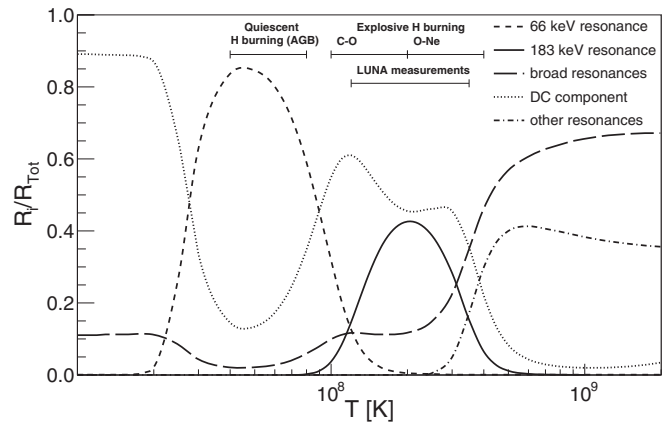

FIG. 10. Fractional contributions to the reaction rate, as a function of temperature, from the DC (dotted line), 183-keV resonance (solid line), tails of the broad 557- and 677-keV resonances (long dashed line), other narrow resonances above the studied energy range (dash-dotted line), and 66-keV resonance (dashed line), which entirely dominates the asymptotic giant branch stars temperature range.

TABLE VIII. Reaction rate for $^{17}O(p,\gamma)^{18}F$.

T (GK)	Lower limit	Recommended value	Upper limit
0.010	3.34×10^{-25}	3.54×10^{-25}	3.75×10^{-25}
0.011	3.55×10^{-24}	3.76×10^{-24}	3.99×10^{-24}
0.012	2.87×10^{-23}	3.05×10^{-23}	3.23×10^{-23}
0.013	1.86×10^{-22}	1.98×10^{-22}	2.09×10^{-22}
0.014	1.01×10^{-21}	1.07×10^{-21}	1.13×10^{-21}
0.015	4.65×10^{-21}	4.93×10^{-21}	5.23×10^{-21}
0.016	1.89×10^{-20}	2.00×10^{-20}	2.12×10^{-20}
0.018	2.25×10^{-19}	2.39×10^{-19}	2.53×10^{-19}
0.020	1.93×10^{-18}	2.05×10^{-18}	2.17×10^{-18}
0.025	1.82×10^{-16}	1.94×10^{-16}	2.07×10^{-16}
0.030	8.64×10^{-15}	9.63×10^{-15}	1.07×10^{-14}
0.040	2.17×10^{-12}	2.51×10^{-12}	2.90×10^{-12}
0.050	6.69×10^{-11}	7.74×10^{-11}	8.95×10^{-11}
0.060	6.73×10^{-10}	7.73×10^{-10}	8.87×10^{-10}
0.070	3.68×10^{-09}	4.17×10^{-09}	4.71×10^{-09}
0.080	1.43×10^{-08}	1.59×10^{-08}	1.76×10^{-08}
0.090	4.59×10^{-08}	4.99×10^{-08}	5.42×10^{-08}
0.100	1.32×10^{-07}	1.41×10^{-07}	1.51×10^{-07}
0.110	3.55×10^{-07}	3.74×10^{-07}	3.95×10^{-07}
0.120	8.98×10^{-07}	9.42×10^{-07}	9.89×10^{-07}
0.130	2.14×10^{-06}	2.24×10^{-06}	2.35×10^{-06}
0.140	4.80×10^{-06}	5.02×10^{-06}	5.25×10^{-06}
0.150	1.01×10^{-05}	1.05×10^{-05}	1.10×10^{-05}
0.160	1.98×10^{-05}	2.07×10^{-05}	2.17×10^{-05}
0.180	6.44×10^{-05}	6.74×10^{-05}	7.05×10^{-05}
0.200	1.73×10^{-04}	1.81×10^{-04}	1.89×10^{-04}
0.250	1.14×10^{-03}	1.19×10^{-03}	1.25×10^{-03}
0.300	4.86×10^{-03}	5.09×10^{-03}	5.33×10^{-03}
0.350	1.90×10^{-02}	2.00×10^{-02}	2.11×10^{-02}
0.400	7.54×10^{-02}	8.09×10^{-02}	8.68×10^{-02}
0.450	2.74×10^{-01}	2.97×10^{-01}	3.23×10^{-01}
0.500	8.45×10^{-01}	9.22×10^{-01}	$1.01 \times 10^{+00}$
0.600	$4.97 \times 10^{+00}$	$5.44 \times 10^{+00}$	$5.94 \times 10^{+00}$
0.700	$1.80 \times 10^{+01}$	$1.97 \times 10^{+01}$	$2.15 \times 10^{+01}$
0.800	$4.73 \times 10^{+01}$	$5.15 \times 10^{+01}$	$5.60 \times 10^{+01}$
0.900	$9.96 \times 10^{+01}$	$1.08 \times 10^{+02}$	$1.17 \times 10^{+02}$
1.000	$1.79 \times 10^{+02}$	$1.94 \times 10^{+02}$	$2.10 \times 10^{+02}$
1.250	$5.04 \times 10^{+02}$	$5.43 \times 10^{+02}$	$5.85 \times 10^{+02}$
1.500	$9.80 \times 10^{+02}$	$1.05 \times 10^{+03}$	$1.13 \times 10^{+03}$
1.750	$1.55 \times 10^{+03}$	$1.66 \times 10^{+03}$	$1.77 \times 10^{+03}$
2.000	$2.16 \times 10^{+03}$	$2.31 \times 10^{+03}$	$2.46 \times 10^{+03}$

the resonance contribution was taken into account for this transition because the corresponding ANC is unknown in literature.

The best fits for the individual transitions are displayed in Fig. 9 together with the experimental data and show a very good overall agreement. The quoted uncertainties for the present analysis in Table VII are statistical uncertainties only and have been obtained from the Monte Carlo procedure described above. For the total uncertainty the systematic uncertainty for stopping power and normalization of primary and common data have to be summed in quadrature to the quoted values.

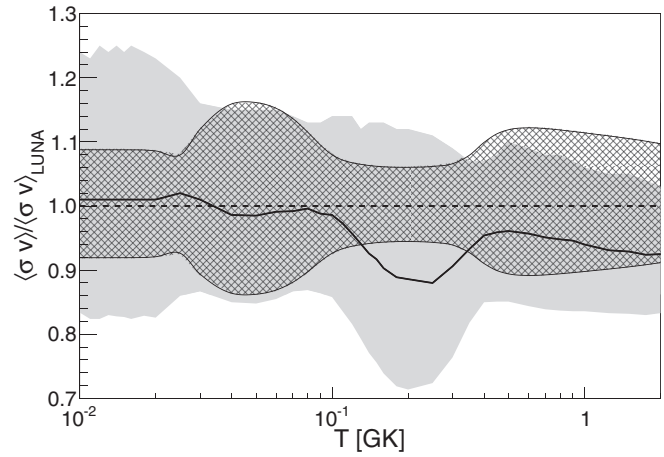

FIG. 11. $^{17}O(p,\gamma)^{18}F$ reaction rate ratio as a function of the temperature. The solid line is the ratio between the rates from a recent compilation [42] and the present work. Hatched and shaded areas represent a 1σ uncertainty on the present and previous rates, respectively. In the relevant nova temperatures $T = 0.1$–0.4 GK, the present study reduces the uncertainty by a factor of 4.

V. REACTION RATE CALCULATION

The astrophysical reaction rate was calculated in an appropriate temperature range using the $^{17}O(p,\gamma)^{18}F$ reaction cross section obtained in the global analysis (see Sec. IV).

The reaction cross section can be expressed as an incoherent sum of the narrow resonances and the combined contribution of the broad resonances and the DC. For the 183-keV resonance and the nonresonant contribution, values from the present work were used. For the other narrow resonances, parameters from Ref. [42] were used.

Figure 10 shows the fractional contributions to the reaction rate from individual contributions. In the window $100 < T < 400$ MK, the reaction rate is nearly entirely dominated by the 183-keV resonance and the DC contribution measured in the present experiment. At $T < 100$ MK, the contribution from the 66-keV resonance becomes increasingly larger and fully dominates the reaction rate at lower temperatures (quiescent H burning).

The reaction rate uncertainty was determined following the Monte Carlo approach of [42], i.e., randomly varying the $\omega\gamma$ values and the fit of the nonresonant part within the respective experimental uncertainties. Table VIII lists the total reaction rates with lower and upper limits. A comparison with rates from Ref. [42] is shown in Fig. 11.

In the temperature region between 100 and 400 MK, the present reaction rates are higher than previously recommended in Ref. [42] because of the higher $\omega\gamma$ of the 183-keV resonance and the larger nonresonant contribution determined in the present work. The uncertainty on the new rate in the same temperature region is decreased by a factor of four with respect to previous recommendations.

In the novae energy range, the present reaction rates differ only slightly from those we presented in Ref. [21] because our data constrain the rate in this energy range. Larger differences, albeit within uncertainties, are found at lower and higher

TABLE IX. Results of nova model calculations. The abundances of ^{18}F, ^{18}O, ^{19}F, and ^{15}N are given in mass fraction.

Model	WD mass ($M_\odot$)	Accreted mass ($10^{-5} M_\odot$)	Core composition	Mixing (%)	T_{peak} (10^8 K)	$^{17}O(p,\gamma)^{18}F$ rate[a]	^{18}F	^{18}O	^{19}F	^{15}N
CO1L	1.00	2.709	CO	25	1.73	PP	1.30×10^6	4.87×10^7	9.57×10^9	8.60×10^3
CO1I	1.00	2.709	CO	25	1.73	IL2010	1.25×10^6	4.68×10^7	9.48×10^9	8.60×10^3
CO1Lu	1.00	2.709	CO	25	1.73	PP upper	1.39×10^6	5.20×10^7	9.76×10^9	8.60×10^3
CO1Ll	1.00	2.709	CO	25	1.73	PP lower	1.22×10^6	4.60×10^7	9.48×10^9	8.60×10^3
CO2L	1.15	1.437	CO	25	2.00	PP	2.63×10^6	1.10×10^6	1.09×10^8	3.03×10^3
CO2I	1.15	1.437	CO	25	2.00	IL2010	2.52×10^6	1.05×10^6	1.07×10^8	3.03×10^3
ONe1L	1.15	2.456	ONe	50	2.28	PP	8.46×10^6	3.64×10^6	5.48×10^8	3.57×10^2
ONe1I	1.15	2.456	ONe	50	2.28	IL2010	8.15×10^6	3.45×10^6	5.38×10^8	3.57×10^2
ONe2L	1.25	1.887	ONe	50	2.48	PP	1.12×10^5	4.90×10^6	1.42×10^7	5.65×10^2
ONe2I	1.25	1.887	ONe	50	2.48	IL2010	1.09×10^5	4.75×10^6	1.40×10^7	5.66×10^2
ONe2Lu	1.25	1.887	ONe	50	2.48	PP upper	1.13×10^5	5.39×10^6	1.43×10^7	5.67×10^2
ONe2Ll	1.25	1.887	ONe	50	2.48	PP lower	1.09×10^5	4.74×10^6	1.41×10^7	5.65×10^2
ONe3L	1.35	0.455	ONe	50	3.13	PP	3.49×10^5	1.56×10^5	1.20×10^6	1.07×10^1
ONe3I	1.35	0.455	ONe	50	3.13	IL2010	3.50×10^5	1.56×10^5	1.20×10^6	1.07×10^1

[a]PP, present paper; PP upper, present paper upper limit; PP lower, present paper lower limit; and IL2010, Ref. [42].

temperatures, mainly because of the inclusion of the recent results of Ref. [20] on the widths of higher-energy resonances. Thus, the reaction rates presented here supersede those of Ref. [21] and represent the most up-to-date results and our recommended values.

VI. ASTROPHYSICAL IMPLICATIONS IN CLASSICAL NOVAE

Stellar evolution theory predicts that stars with initial mass below $\sim 8\ M_\odot$ produce WDs whose core composition is a mixture of C and O (CO WD) [43,44]. On the other hand, stars with slightly larger initial mass (8–10 $M_\odot$) may end their life as WDs with a core made of O and Ne (ONe WD) [45–47].

Accurate spectroscopic observations of classical novae [9] show a substantial enhancement of intermediate-mass elements (such as C-N-O and Ne in some cases) in the ejected material compared to solar abundances. This is generally considered a signature of a deep mixing episode occurred during the explosive phase [48,49]. Note that since the H burning during nova explosions is mainly powered by the hot CNO cycle, the increase of the envelope abundance of C+N+O gives rise to more violent bursts.

In order to evaluate the influence of the reaction rate on the expected nucleosynthesis products, a set of nova models were investigated (see Ref. [5] for details on the adopted 1-D hydrodynamic SHIVA code): CO WDs with masses 1.0 and 1.15 $M_\odot$ as well as ONe WDs with masses 1.15, 1.25, and 1.35 $M_\odot$. For each pair (WD mass, core composition), two nova models were computed with different reaction rates of the $^{17}O(p,\gamma)^{18}F$ reaction: our recommended rate and the one from Ref. [42], respectively. In two cases, the $M = 1.0\ M_\odot$ CO WD and the $M = 1.25\ M_\odot$ ONe WD, we have also computed two additional models using the lower and the upper limits of the reaction rate. Table IX summarizes the parameters characterizing each model as well as the predicted abundances of the most relevant isotopes in the ejected material. The peak temperature (T_{peak}) is the maximum temperature attained during the outburst at the bottom of the H-rich envelope, while the mixing parameter refers to the amount of core composition material mixed into the accreted H-rich envelope (values in percentages of the envelope mass). In the cases of ^{18}F and ^{18}O, the values at $t = 1$ h after the peak temperature are reported. Note that at that time, the synthesis of the various nuclei is frozen, except for the residual β decays.

Note that all the T_{peak} values fall into the range of temperatures for which this experiment provides a major contribution to the present determination of the $^{17}O(p,\gamma)^{18}F$ reaction rate. The abundances obtained with different $^{17}O(p,\gamma)^{18}F$ rates differ by only a few percent. By comparing the models computed with the new rate to the ones computed with Ref. [42], we found a maximum variation for the ^{18}O abundance of 5%. Similar differences are found for ^{18}F, while ^{19}F differs by less than 2%. Finally, the uncertainties in the new reaction rate cause maximum variations of ^{18}O and ^{18}F of the order of 10%. The ^{15}N abundance is practically unaffected by changing the rate within the experimental uncertainty.

VII. CONCLUSIONS

The $^{17}O(p,\gamma)^{18}F$ reaction has been studied in a wide energy region ($E_{c.m.} = 160$ to 370 keV) appropriate to explosive hydrogen burning in classical novae. The reaction cross section was measured using both prompt γ-ray detection and activation approaches. Results from the nonresonant reaction contributions have been analyzed in a global fit and lead to a total astrophysical S factor $S(0) = 5.0 \pm 0.3$ keV barn. The strength of the $E_{c.m.} = 183$ keV resonance, $\omega\gamma = 1.67 \pm 0.12\ \mu$eV, has been determined with the highest precision to date and was found to dominate, together with the DC component, the astrophysical reaction rate at temperatures $0.1 < T < 0.4$ GK, relevant to novae explosions. A global fit to our experimental data and other data from the literature

has led to an improved recommended reaction rate. The abundances of key isotopes such as ^{18}F, ^{18}O, ^{19}F, and ^{15}N have been evaluated through nova models calculations and are now obtained with a precision of 10%, i.e., sufficient to put firmer constraints on observational features of novae nucleosynthesis. The results presented in this study are now sufficiently precise for nova model calculations.

ACKNOWLEDGMENTS

The authors thank the INFN mechanical workshop, electronics, and chemical laboratories of LNGS. A.C. acknowledges financial support by Fondazione Cassa di Risparmio di Padova e Rovigo. A.D.L. acknowledges financial support by MIUR (FIRB RBFR08549F). J.J. acknowledges support from the MEC Grant AYA2010-15685 and the ESF EUROCORES Program EuroGENESIS through the EUI2009-04167 grant. Financial support by OTKA K101328, K108459, DFG (BE 4100/2-1), and NAVI (HGF VH-VI-417) is also gratefully acknowledged.

APPENDIX: PRIMARY TRANSITIONS

All the remaining fits of the primary transitions are shown in Fig. 12.

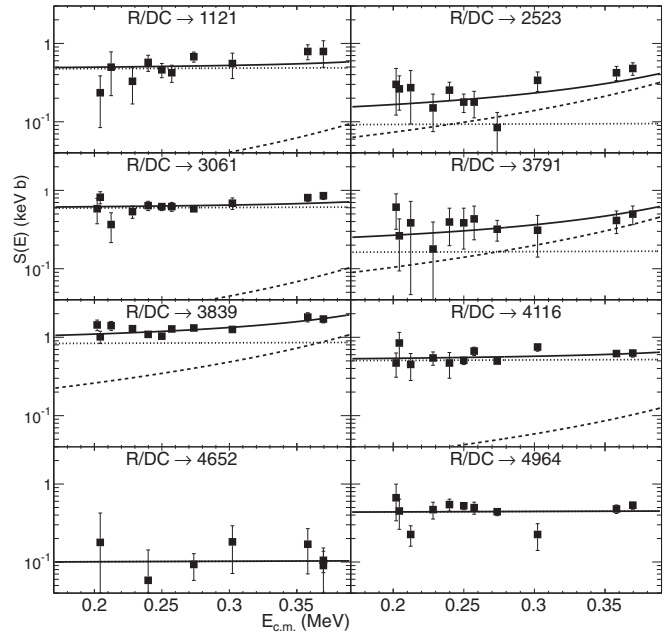

FIG. 12. Fits of the S factor of the ^{17}O$(p,\gamma)^{18}$F primary γ-ray transition to the different bound states in ^{18}F. Only statistical uncertainties are shown. The lines are coded as in Fig. 9.

[1] M. F. Bode and A. Evans (eds.), *Classical Novae*, 2nd ed., Cambridge Astrophysics Series No. 43 (Cambridge University Press, Cambridge, 2008).
[2] J. José and M. Hernanz, J. Phys. G **34**, 431 (2007).
[3] J. José and S. Shore, in Ref. [1], p. 252.
[4] S. Starrfield, C. Iliadis, and W. R. Hix, in Ref. [1], p. 77.
[5] J. José and M. Hernanz, Astroph. J. **494**, 680 (1998).
[6] D. Tilley, H. Weller, C. Cheves, and R. Chasteler, Nucl. Phys. A **595**, 1 (1995).
[7] A. Kovetz and D. Prialnik, Astroph. J. **477**, 356 (1997).
[8] J. José, M. Hernanz, and C. Iliadis, Nucl. Phys. A **777**, 550 (2006).
[9] R. D. Gehrz, J. W. Truran, R. E. Williams, and S. Starrfield, Publ. Astr. Soc. Pac. **110**, 3 (1998).
[10] S. Amari, X. Gao, L. R. Nittler, E. Zinner, J. José, M. Hernanz, and R. S. Lewis, Astroph. J. **551**, 1065 (2001).
[11] S. Amari, New A. Rev. **46**, 519 (2002).
[12] R. Diehl, Rep. Prog. Phys. **76**, 026301 (2013).
[13] C. Rolfs, Nucl. Phys. A **217**, 29 (1973).
[14] C. Rolfs and W. Rodney, *Cauldrons in the Cosmos* (University of Chicago Press, Chicago, 1988).
[15] C. Fox, C. Iliadis, A. E. Champagne, A. Coc, J. José, R. Longland, J. Newton, J. Pollanen, and R. Runkle, Phys. Rev. Lett. **93**, 081102 (2004).
[16] C. Fox, C. Iliadis, A. E. Champagne, R. P. Fitzgerald, R. Longland, J. Newton, J. Pollanen, and R. Runkle, Phys. Rev. C **71**, 055801 (2005).
[17] A. Chafa, V. Tatischeff, P. Aguer, S. Barhoumi, A. Coc, F. Garrido, M. Hernanz, J. José, J. Kiener, A. Lefebvre-Schuhl, S. Ouichaoui, N. de Séréville, and J.-P. Thibaud, Phys. Rev. C **75**, 035810 (2007); Phys. Rev. Lett. **95**, 031101 (2005); **96**, 031101(E) (2006).
[18] J. R. Newton, C. Iliadis, A. E. Champagne, J. M. Cesaratto, S. Daigle, and R. Longland, Phys. Rev. C **81**, 045801 (2010).
[19] U. Hager, L. Buchmann, B. Davids, J. Fallis, B. R. Fulton, N. Galinski, U. Greife, D. A. Hutcheon, D. Ottewell, A. Rojas, C. Ruiz, and K. Setoodehnia, Phys. Rev. C **85**, 035803 (2012).
[20] A. Kontos, J. Görres, A. Best, M. Couder, R. deBoer, G. Imbriani, Q. Li, D. Robertson, D. Schürmann, E. Stech, E. Uberseder, and M. Wiescher, Phys. Rev. C **86**, 055801 (2012).
[21] D. A. Scott *et al.*, Phys. Rev. Lett. **109**, 202501 (2012).
[22] A. Formicola *et al.*, Nucl. Instrum. Methods Phys. Res., Sect. A **507**, 609 (2003).
[23] A. Caciolli *et al.*, Eur. Phys. J. A **48**, 144 (2012).
[24] A. Caciolli *et al.*, Eur. Phys. J. A **39**, 179 (2009).
[25] S. Agostinelli *et al.*, Nucl. Instr. Meth. A **506**, 250 (2003).
[26] G. Imbriani *et al.*, Eur. Phys. J. A **25**, 455 (2005).
[27] B. Limata *et al.*, Phys. Rev. C **82**, 015801 (2010).
[28] G. R. Gilmore, *Practical Gamma-Ray Spectrometry*, 2nd ed. (Wiley-VCH Verlag, Weinheim, Germany, 2008).
[29] "Nudat2", http://www.nndc.bnl.gov.
[30] G. Gyürky *et al.* (LUNA Collaboration), Phys. Rev. C **75**, 035805 (2007).
[31] M. Laubenstein, M. Hult, J. Gasparro, D. Arnold, S. Neumaier, G. Heusser, M. Köhler, P. Povinec, J.-L. Reyss, M. Schwaiger, and P. Theodórsson, Appl. Radiat. Isot. **61**, 167 (2004).

[32] M. Boswell *et al.*, IEEE Trans. Nucl. Sci. **58**, 1212 (2011).
[33] J. Biersack and J. Ziegler, *Transport of Ions in Matter: TRIM Program Version 2008* (IBM Research, New York, and Hahn Meitner Institute, Berlin, 2008).
[34] C. Iliadis, *Nuclear Physics of Stars* (Wiley-VCH Verlag, Weinheim, Germany, 2007).
[35] C. Rolfs, A. Charlesworth, and R. Azuma, Nucl. Phys. A **199**, 257 (1973).
[36] C. Iliadis, R. Longland, A. E. Champagne, A. Coc, and R. Fitzgerald, Nucl. Phys. A **841**, 31 (2010).
[37] C. Ko, J. Borysowicz, A. Becke, and D. Sprung, Nucl. Phys. A **319**, 175 (1979).
[38] G. D'Agostini, Nucl. Instr. Meth. A **346**, 306 (1994).
[39] D. Schürmann, L. Gialanella, R. Kunz, and F. Strieder, Phys. Lett. B **711**, 35 (2012).
[40] U. Hager (private communication).
[41] J. Newton, Ph.D. thesis, University of North Carolina, Chapel Hill, 2010.
[42] C. Iliadis, R. Longland, A. E. Champagne, and A. Coc, Nucl. Phys. A **841**, 251 (2010).
[43] S. A. Becker and I. Iben, Jr., Astroph. J. **232**, 831 (1979).
[44] I. Dominguez, A. Chieffi, M. Limongi, and O. Straniero, Astroph. J. **524**, 226 (1999).
[45] I. Dominguez, A. Tornambe, and J. Isern, Astroph. J. **419**, 268 (1993).
[46] C. Ritossa, E. Garcia-Berro, and I. Iben, Jr., Astroph. J. **460**, 489 (1996).
[47] L. G. Althaus, A. H. Córsico, J. Isern, and E. García-Berro, Astron. Astrophys. Rev. **18**, 471 (2010).
[48] J. Casanova, J. José, E. García-Berro, A. Calder, and S. N. Shore, Astron. Astrophys. **527**, A5 (2011).
[49] J. Casanova, J. José, E. García-Berro, S. N. Shore, and A. C. Calder, Nature (London) **478**, 490 (2011).